LASER & PHOTONICS REVIEWS
www.lpr-journal.org

Remote 3D Imaging and Classification of Pelagic Microorganisms with A Short-Range Multispectral Confocal LiDAR

Joaquim Santos, Hans H. Jakobsen, Paul M. Petersen, and Christian Pedersen**

Plankton is essential to maintain healthy aquatic ecosystems since it influences the biological carbon pump globally. However, climate change-induced alterations to oceanic properties threaten planktonic communities. It is therefore crucial to monitor their abundance to assess the health status of marine ecosystems. In situ optical tools unlock high-resolution measurements of sub-millimeter specimens, but state-of-the-art underwater imaging techniques are limited to fixed and small close-range volumes, requiring the instruments to be vertically dived. Here, a novel scanning multispectral confocal light detection and ranging (LiDAR) system for short-range volumetric sensing in aquatic media is introduced. The system expands the inelastic confocal principle to multiple wavelength channels, allowing the acquisition of 4D point clouds combining near-diffraction limited morphological and spectroscopic data that is used to train artificial intelligence (AI) models. Volumetric mapping and classification of microplastics is demonstrated to sort them by color and size. Furthermore, in vivo autofluorescence is resolved from a community of free-swimming zooplankton and microalgae, and accurate spectral identification of different genera is accomplished. The deployment of this photonic platform alongside AI models overcomes the complex and subjective task of manual plankton identification and enables non-intrusive sensing from fixed vantage points, thus constituting a unique tool for underwater environmental monitoring.

1. Introduction

Despite its microscopic size, planktonic organisms play a crucial role in maintaining the delicate balance of Earth's ecosystems. Both phytoplankton and zooplankton form the foundation of marine food webs, thus serving as primary food sources for countless marine species. In particular, phytoplankton significantly contributes to global oxygen production through photosynthesis,[1] playing a critical role in regulating the planet's atmospheric content. Nevertheless, climate change-induced shifts in the oceans' properties[2] pose a severe threat to planktonic communities and their functions, directly impacting their populations on local and global scales,[3] and consequently disrupting marine ecosystems. These changes have cascading effects on the entire food web, affecting fish stocks, marine mammals, and ultimately, human communities that rely on healthy oceans for sustenance and economic livelihoods.[4] In this sequence, monitoring the biodiversity, abundance, and distribution of plankton is essential to get insights into the status and functioning of marine ecosystems, serving as an early indicator of the impact of environmental changes.[5]

Optical and photonic tools[6] play a key role in advancing our understanding of plankton dynamics and ecology, as they provide non-intrusive and high-resolution quantitative measurements that can replace manual sampling techniques using nets.[7] These techniques can be combined with automated pattern recognition and classification, such as artificial neural networks.[8,9] Since the concentration of planktonic organisms decreases with size, it is practically impossible to sample the full ecosystem using a sole sampling strategy.[5] Historically, spaceborne remote sensing with Light Detection and Ranging (LiDAR) platforms has unlocked large spatial scale descriptions of plankton distributions, for instance of phytoplankton biomass cycles[10] and diel vertical migrations of wide zooplankton conglomerates within the water column.[11] Nevertheless, due to the coarse lateral and axial resolutions of these long-range systems (in the several meters order[12]) it is unattainable to sample individual specimens and thus capture the sheer diversity of

J. Santos, P. M. Petersen, C. Pedersen
DTU Electro
Department of Electrical and Photonics Engineering
Technical University of Denmark
Frederiksborgvej 399, 4000 Roskilde, Denmark
E-mail: joasan@dtu.dk; chrp@dtu.dk
H. H. Jakobsen
Department of Ecoscience
Aarhus University
Frederiksborgvej 399, 4000 Roskilde, Denmark

The ORCID identification number(s) for the author(s) of this article can be found under https://doi.org/10.1002/lpor.202301291

DOI: 10.1002/lpor.202301291

plankton, whose sizes span across several orders of magnitude from tens of nanometers to meter scales.[13]

To resolve individual planktonic organisms, adequate resolution is required on the lateral, axial, and temporal dimensions. In situ platforms, deployed either from above the water's surface[14] or directly underwater,[5,15] have the potential to achieve the required resolution to detect single sub-millimeter organisms. The most widely used techniques for plankton surveying include advanced imaging systems such as imaging flow cytometry,[16] digital holography,[17] dark-field illumination,[18] underwater video recording,[19] and more recently underwater microscopy.[20] Although these systems can sample down to the single microorganism level, they typically require the particles to pass through small and fixed close-range interrogation volumes, hence requiring the whole instrument to be scanned/dived in order to produce spatial distributions,[21] which inevitably stirs the dynamics of the organisms due to water displacement. Moreover, these imaging techniques are challenged by similarities in optical and morphological characteristics among different plankton species, limiting the taxonomic resolution[22] and making automated identification with high accuracy a longstanding challenge. A summarized comparison of state-of-the-art optical methodologies is reported in refs. [5] and [21].

Laser-induced autofluorescence emerging from naturally occurring pigments in plankton can be harnessed as an additional cue to support identification, as it contains molecular information that further improves specificity. Phytoplankton exhibits distinctive autofluorescence peaking at a wavelength $\lambda \approx 685$ nm due to the presence of chlorophyll-*a* molecules.[23,24] Similarly, some zooplankton species also emit characteristic fluorescence when excited with blue light.[25] Hyperspectral Scheimpflug LiDAR systems have been recently developed to capture both elastic and inelastic scattering signatures from aquatic biota,[12] using a collimated blue laser beam for excitation and triangulation for time and axially-resolved spectral measurements. This technology has been used to demonstrate range-resolved detection of dye-tagged sub-millimeter zooplankton[12] and spectral classification of different microalgae species.[26] Owing to the non-imaging nature of this technique in the lateral direction, only range-resolved spectroscopic information is acquired. Nonetheless, autofluorescence is not specific enough per se and therefore must be complemented with morphological information, such as shape, size, and other geometrical descriptors,[8] if a high-taxonomic resolution is desired. The combination of 2D spatial data with spectral information at a pixel level is possible with hyperspectral imaging.[27–29] This approach, when combined with machine learning models, trained on spectral features alone[30] or combined with spatial information,[31] enables the classification of, for e.g., of microplastics,[32] microalgae,[33] and aquatic megafauna.[34] However, being a wide-field imaging methodology, conventional hyperspectral imaging is unable to provide depth information, being therefore incompatible with profiling in the water column required to map volumetric distributions.

In this work, we introduce a scanning multispectral confocal LiDAR for volumetric sensing of laser-induced autofluorescence in aquatic media. This system expands the inelastic confocal imaging principle[21] to multiple wavelength channels by replacing the single detector with a custom spectrograph and a 16-channel high-sensitivity detector array. This addition unlocks a wavelength dimension which, combined with a point-scanner and a remote focusing module, allows the acquisition of 4D point clouds integrating high-resolution volumetric spatial data with voxel-level fluorescence spectrum. This data structure yields unprecedentedly rich morphological and spectroscopic data that, in combination with artificial intelligence (AI) models, can be used for in situ and automated 3D classification of objects within the sensor's field-of-view (FOV). The measurement principle is similar to confocal tomography[35] and confocal microscopy[36] across multiple wavelength channels:[37,38] the confocality between the excitation laser probe and a conjugated pinhole aperture spatially rejects out-of-focus contributions from scattered and background light, and allows to achieve near diffraction-limited resolutions. In the context of underwater imaging, this inherent feature alleviates the challenges of scattering and absorption from both water molecules and suspended matter.[39,40]

We demonstrate, for the first time to our knowledge, the implementation of short-range remote multispectral confocal imaging in a lab setup and spectral classification of pelagic microorganisms. We start by quantifying the system's resolution from experimental measurements of the axial weighting functions and lateral point spread functions (PSFs). Afterwards, we demonstrate multispectral underwater imaging of an axially confined layer of micrometer-sized fluorescent polyethylene beads. With this experiment, we show the capability of our system for accurate mapping, classification, and subsequent determination of color and size distributions of microplastics[41] in a column of water. Ultimately, we carried out an underwater non-invasive survey of a community of four free-swimming copepod species and free-floating microalgae using the multispectral confocal LiDAR sensor. We then prove accurate pixel-wise spectral classification according to species using an ensemble machine learning algorithm (adaptive boosting, AdaBoost). Our results demonstrate that this underwater LiDAR instrument holds great potential for advancing our understanding of plankton ecology through remote and non-intrusive measurements. Thus the sensor can potentially contribute to more effective marine ecosystem management and environmental monitoring of e.g., coastal waters, in short-range distances up to around 5 meters.

2. Multispectral Confocal LiDAR

A schematic diagram of the developed inelastic multispectral confocal LiDAR is presented in **Figure 1**. A 445 nm Laser Diode (LD, Toptica iBeam-smart 445-s) is used as excitation source to match the transmission window of pure water[42] and to promote efficient autofluorescence emission from fluorophores typically present in aquatic biota, such as chlorophyll pigments.[12] The laser module is operated in continuous wave (CW) mode and outputs a high-quality collimated Gaussian beam (TEM_{00}, $M^2 < 1.1$), with a software-controllable power of up to 100 mW. The excitation plane wave is reflected by a long-pass dichroic mirror (DM, Thorlabs DMLP490) with a cut-on wavelength of 490 nm to separate excitation from inelastic emission. The beam is then tightly focused and the spot re-imaged onto a near-diffraction limited waist at an underwater probing distance z_0 by a pair of achromatic doublet lenses L_1 (f = 19 mm, Thorlabs AC127-019-A) and L_2 (f = 150 mm, Thorlabs AC254-150-A) in a telescope configuration. Motorized mechanical remote focusing is implemented

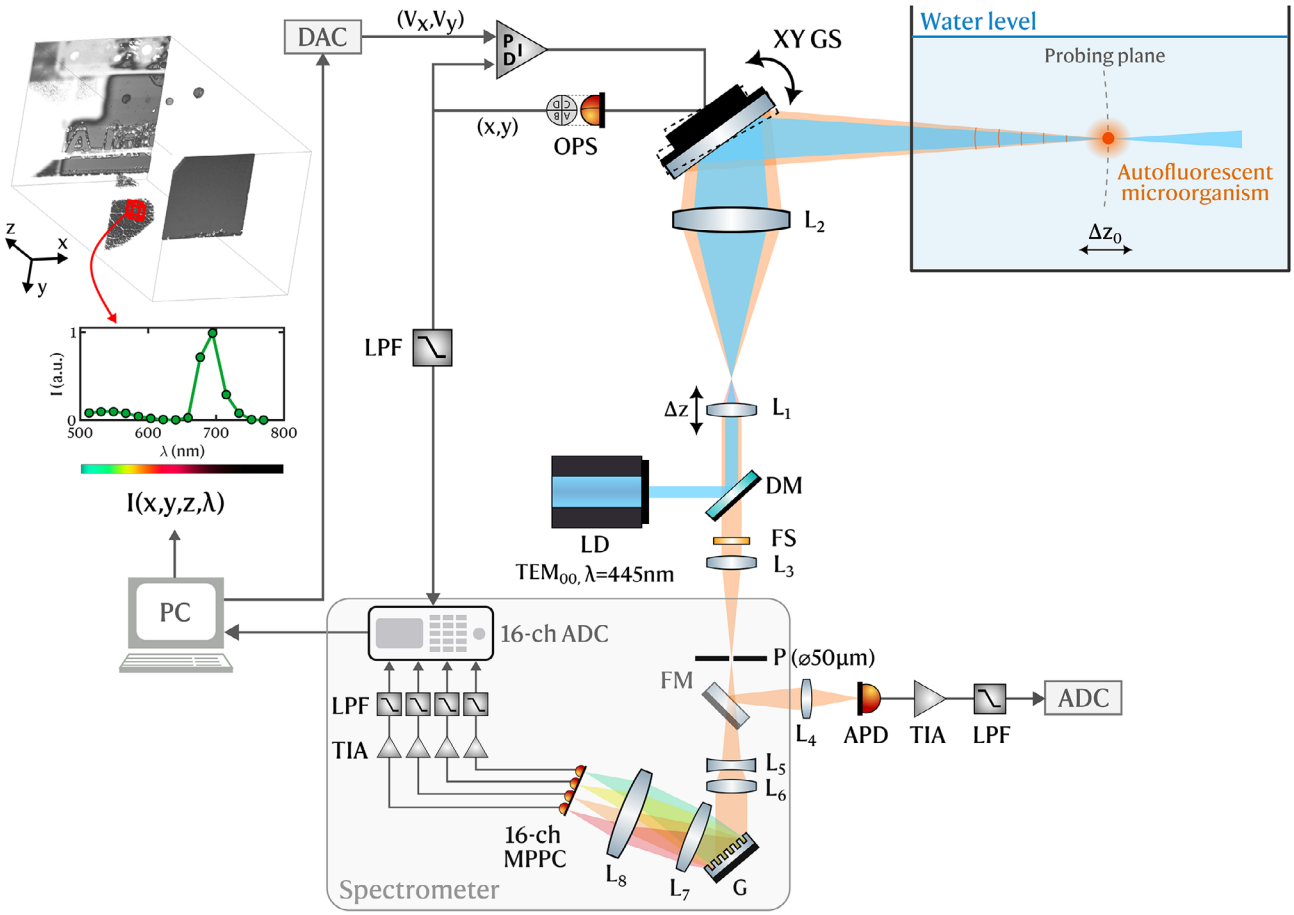

Figure 1. Schematic diagram of the multispectral confocal LiDAR optical setup focused at a probing distance z_0 in an aquatic medium.

by mounting L_1 on a resonant piezoelectric z-translation stage (Thorlabs ELL20/M) to automatically scan z_0.

Due to the confocal detection scheme, both the excitation and emission channels are coaxially shared (monostatic system), therefore securing a consistent overlap in FOV between the two optical paths and a common optical magnification irrespective of z_0. Accordingly, the laser-induced autofluorescence (diverging spherical wavefront) is epi-collected by the objective lens L_2 and re-collimated by L_1 upon backward propagation through the telescope pair. The inelastic signal is then transmitted through the DM and filtered by an emission filter set (FS) consisting of a pair of long-pass interference filters with 500 nm cut-on wavelength (Thorlabs FELH0500), before being focused through a 50 m diameter pinhole (P) by an achromatic doublet lens L_3 (f = 75 mm, Thorlabs AC254-075-A). The circular aperture is placed at a plane conjugated to the laser probe and its size is chosen to approximately match the exp(-2) waist diameter of the excitation beam after back-propagation to the pinhole space, thus attaining confocal imaging with narrow depth-of-focus (DoF) and spatially suppressing out-of-focus and scattered photons.[36,43] Concurrently, the pinhole also functions as an input aperture for a multispectral detection system.

A fast photon-counting custom grating spectrometer is designed to record spectrally-resolved data in the visible wavelength interval from around 505 to 780 nm, therefore matching the range of interest for autofluorescence detection from zooplankton and phytoplankton.[25] The spatially coherent optical field is first expanded by a plano-convex lens L_5 (f = -25 mm, Thorlabs LC1054-A) and collimated into a polychromatic plane wave by an achromatic doublet lens L_6 (f = 80 mm, Thorlabs AC254-080-A), to enhance the spectral resolving power of the spectrograph. Afterward, a ruled reflective diffraction grating (G, Thorlabs GR20-1205, 1200 grooves/mm), at an incidence angle of 45°, diffracts the light with wavelength information encoded in the angle. Finally, the spectrum is imaged onto a 16-channel multi-pixel photon counter (MPPC) linear array (Hamamatsu C13368-3050EA-16) by a pair of doublet achromatic lenses L7 (f = 350 mm, Thorlabs AC254-350-A) and L8 (f = 200 mm, Thorlabs ACT508-200-A). The focusing system is divided into two lenses with an equivalent focal length f = 153.5 mm to reduce the field curvature on the planar detector. The detector consists of an array of 3×3 mm^2 macropixels, each comprised of a high-density matrix of 50×50 m^2 avalanche photodiodes operated in Geiger-mode, with 5 MHz bandwidth, and featuring low noise-equivalent power (1.2 fWHz$^{-1/2}$) and high photoelectric conversion sensitivity (10^9 VW^{-1}) required for low-light imaging at short pixel dwell/integration times. Each channel has an integrated transimpedance amplifier (TIA) whose analog outputs are connected to a 16-channel and 16-bit Analog-to-digital Converter (ADC, D-tacq ACQ425ELF-16-2000-16-HG) with

simultaneous sampling of up to a frequency of $f_s = 2$ MHz/channel. A first-order low-pass electronic filter (LPF) with a cut-off frequency $f_c = 360$ kHz limits the input bandwidth to each channel to restrain the integrated noise and prevent aliasing, by conforming with the Nyquist sampling theorem ($f_c < f_s/2$). Under this scheme, a pixel dwell time of down to around 2.8 s (i.e., up to 360 000 spectra per second) is permissible without incurring in electronic blurring. The wavelength and intensity calibration of the confocal spectrometer are described in Note S1 (Supporting Information).

A single-element avalanche photodiode (APD, Laser Components A-CUBE-S500-01) is used for pinhole alignment and to ensure a common focus for the excitation and emission paths. For this purpose, a folding mirror (FM) is mounted after the pinhole to reflect the transmitted light, which is then re-imaged by a doublet achromatic lens L_4 (Thorlabs AC127-025-AB) onto the APD. By integrating all spectra onto a single detector, the best comprehensive pinhole position is determined when accounting for the added effects of chromatic and spherical aberrations.

To conclude, post-objective transverse scanning is implemented with a dual-axis galvanometer scanner (XY GS, Thorlabs QS20XY-AG) to obtain 2D images with high spatial resolution through spatial convolution of the probe through the scene. As the full-scanning periods are much longer than the photon travel times, the GS simultaneously scans the excitation beam and de-scans the inelastic emission while conserving the pinhole-laser probe conjugation.[21] The azimuth (x) and elevation (y) angles of the scanner are independently controlled by voltage-driving waves generated by a Digital-to-analog (DAC) board (National Instruments USB-6341, 16 bits, 840 kHz/channel) fed to two Proportional-integral-derivative (PID) servo drivers. An optical position sensor (OPS) provides real-time feedback on the instantaneous angular position of each axis of the galvanometer for closed-loop operation. Since position information is required to index the signals within the FOV during image reconstruction, the fast-axis (x) position signal produced by the OPS is sampled by the 16-channel ADC and the images are reconstructed pixel-by-pixel (point-scanning system). Therefore, only 15 channels of the MPPC are effectively used to acquire spectroscopic data. All the processing is performed a posteriori in MATLAB. The resulting data structures are 4D, with high-spatial resolution volumetric data consisting of a stack of near-diffraction limited xy images over axially-selective narrow slices at probing distances z_0, alongside wavelength-resolved data, i.e., an emission spectrum for each voxel: $I(x, y, z, \lambda)$. Because all spectral channels are acquired simultaneously, the spectral images are fully spatially overlapped. The information-rich data obtained by this volumetric imaging spectrometer can afterward be used to carry out pixel-wise classification and categorize different objects within the FOV using AI trained, for instance, on spectral features, which would otherwise not be possible with a single-band system.[21]

3. Results

3.1. Axial and Lateral Resolution

Figure 2a,b shows the axial weighting functions obtained with two fluorescent microscope slides, a yellow slide (Thorlabs FSK3) and a red slide (Thorlabs FSK6), respectively, as a function of the position along the optical axis, z, and the wavelength, λ, for six different underwater probing distances, z_0, and after deconvolution as described in Section 5. Along the z-axis, the Lorentzian-shaped curves fitted to the experimental points describe the relative inelastic signal returning to each channel of the MPPC, as a function of the absolute distance to the focal plane of the system, $|z - z_0|$, defined by the position of L_1, z_{piezo}. The well-defined and narrow peaks centered at z_0 portray the optical sectioning inherent to the confocal detection scheme with narrow DoF. Each spatial data point has an associated spectrum whose shape is preserved at each z-position, irrespective of the position along the probe. The normalized spectrum of each slide at the peak of the weighting functions is presented in Figure 2c in solid lines, plotted against the spectrum acquired with a fiber-coupled spectrometer (Avantes AvaSpec-2048FT-SPU, 1.2 nm spectral resolution) in air, shown as shaded regions. While for the yellow slide the spectrum is similar for all underwater distances, for the red slide there is a systematic change in shape for $\lambda > 600$ nm as the underwater distance changes, likely due to a larger absorption coefficient of water in this wavelength range[42] and therefore a more accentuated attenuation as the optical path in water increases. In all cases, there is a good concordance between the spectrum measured with the confocal LiDAR and the spectrometer, indicating a successful calibration of the multispectral system.

The axial resolution of the system, δz, is estimated from Lorentzian fits to the λ-integrated weighting functions, portrayed in Figure 2d. Furthermore, each underwater probing distance z_0 can be traced back to a particular position of L_1, z_{piezo}, as depicted in Figure 2e. The relation between the two previous variables is modeled using ray optics[21] to obtain a ranging equation that maps an arbitrary z_{piezo} to a specific underwater focal distance z_0, and that is used throughout the rest of the manuscript.

Since sensing is performed in an absorptive medium, the dissipated energy increases as the total underwater distance, $2(z_0 - d_{air})$, increases. The net result is a decrease in the area under the curve (AUC) of the weighting functions, which would otherwise remain approximately constant had the energy been preserved in the propagation medium. The attenuation coefficient of the medium, α, is thus computed for each wavelength channel by fitting the AUC versus z_0 plots to an exponential loss function, i.e., Beer's law, $AUC(z_0, \lambda) = A \cdot \exp[-\alpha(\lambda)(z_0 - d_{air})]$, where A and α are fitting parameters, $d_{air} = 359$ mm is optical path length in air, and the AUC is calculated by integrating the Lorentzian weighting functions. The detailed results are included in Figure S6 (Supporting Information). The attenuation coefficient as a function of the wavelength is shown in Figure 2f, determined from the weighting functions obtained for the yellow fluorescent slide (FSK3). Only the first seven spectral channels (≈510–620 nm) are depicted as the signal-to-noise ratio (SNR) was insufficient for longer wavelengths. The attenuation coefficient reaches a minimum $\alpha(\lambda = 548.9nm) = 0.224m^{-1}$ and monotonically increases until $\alpha(\lambda = 622.1nm) = 0.626m^{-1}$, which corroborates the change in the emission spectrum of the red slide in Figure 2c for longer wavelengths and as the underwater distance increases. These values are similar to the reported in ref. [21] and slightly above the absorption values reported for pure water,[42] whose minimum occurs at 417.5 nm. The differences might be justified by the tap water content versus pure water and

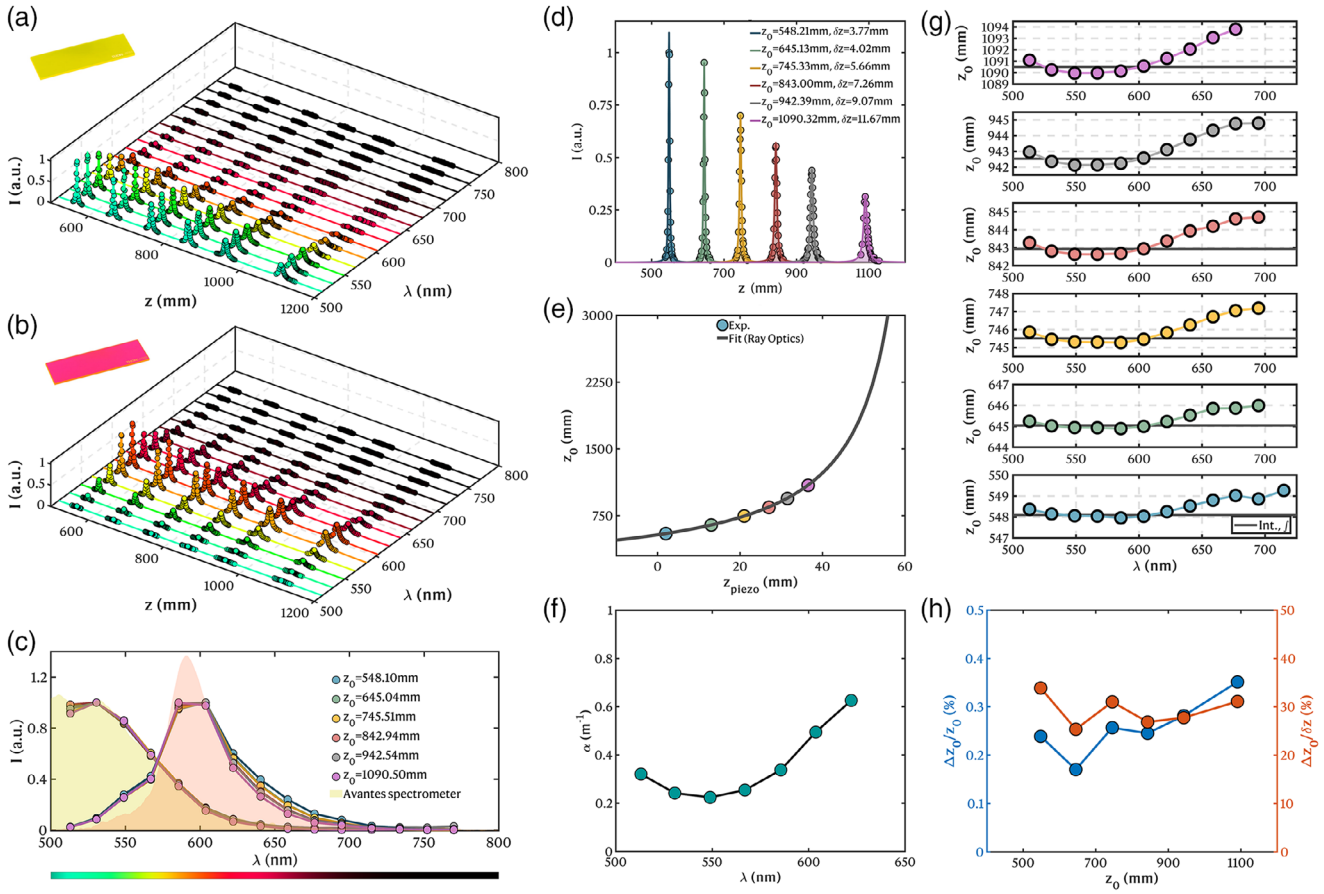

Figure 2. Experimental underwater axial weighting functions of the multispectral confocal LiDAR system. a, b) Weighting functions measured with a yellow (FSK3) and red (FSK6) fluorescent slides as a function of the axial position, z, and the wavelength, λ, at six probing distances. c) Normalized spectrum of both slides as obtained with the confocal LiDAR spectrum at the peak of the weighting function at the six measured distances. The shaded areas represent the spectrum measured with a high-resolution fiber-coupled spectrometer. d) Weighting functions for the yellow slide on the integrated channel, obtained by integrating (a) along λ. e) Integrated probing distance, z_0, as a function of the position of L_1, z_{piezo}, fitted with a ray optics model describing the ranging calibration of the system. f) Attenuation coefficient of the aquatic medium as a function of the wavelength. Each point was computed from the exponential decay in the AUC of the weighting functions obtained with the yellow slide. g) Probing distance as a function of the wavelength for the six z_{piezo}. The solid dark line marks the probing distance of the integrated wavelength channel, z_0. h) Ratio between the shift in focusing distance, Δz_0, and the probing distance, z_0, and the FWHM, δz, of the integrated weighting functions.

the accounting of scattering effects in the estimates with our confocal LiDAR system.

We also investigated the effects of chromatic aberrations arising from dispersion in the lenses when a broad range of wavelengths is detected, which translates into a shift in the probing distance as a function of the wavelength. Figure 2g shows the location of the peak of the weighting functions, z_0, as a function of λ for all the measured underwater distances. For all positions, the probing distance reaches a minimum at $\lambda = 548.9$ nm, and then systematically increases with wavelength. To conclude about the relative impact of chromatic aberrations, we compare the total shift in the focusing distance, Δz_0, with both the probing distance, z_0, and the FWHM, δz, of the integrated weighting functions in Figure 2h. In the former case, the shift in the focal plane is negligible, corresponding to less than 0.4% of the probing distance; as for the latter, the chromatic aberration effects account for a shift in the probing distance of less than 40% of δz, i.e., of the DoF. Hence, since the focal displacement is smaller than the FWHM of the axial weighting functions, we can conclude that chromatic aberrations do not substantially limit the performance of the system. It is noteworthy that the captured effect is the compound of all elements in the optical train between the target and the confocal pinhole. We opted to employ achromatic doublet lenses to achieve good chromatic and spherical performance.

The lateral resolution was estimated by probing the PSF with 22–27 m-diameter red fluorescent beads.[44] **Figure 3a** shows images of a bead for an underwater probing distance $z_0 \approx 548.5$mm ($z_{piezo} = 2.0$ mm), as a function of the wavelength (horizontal axis) and the z-position along the probe (vertical axis). The wavelength-integrated xy and xz profiles are represented on the right-hand side. As the bead is moved away from the focal plane, the return signal fades and its image becomes blurred, due to spatial filtering by the pinhole and a reduction of the local power density of the excitation laser outside the waist. From the integrated xz profile, one can visualize the spatial confinement of the

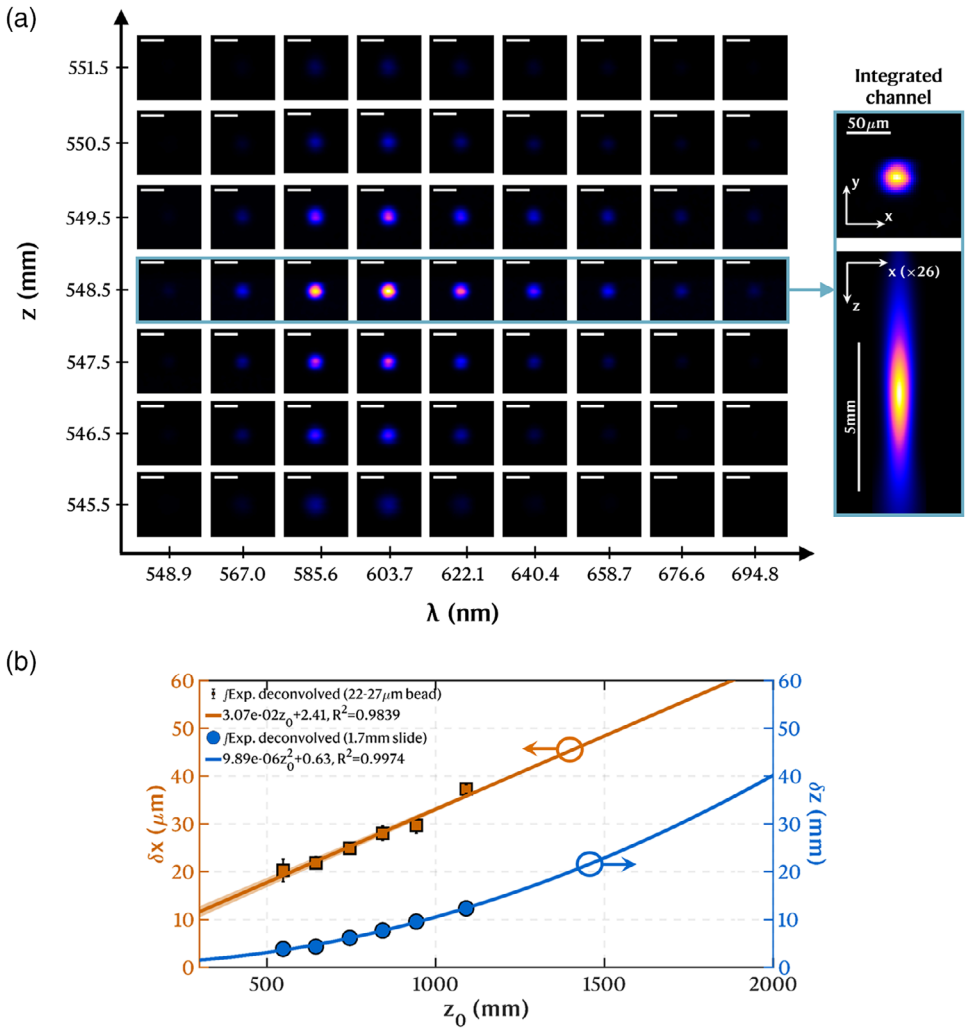

Figure 3. Empirical estimation of the resolution of the confocal system. a) Example of a 4D PSF acquired with a 22–27 m bead as probe. Each image is 50 × 50 and was acquired with a pixel dwell time of 4.44 s at an underwater probing distance $z_0 \approx 548.5$ mm. Scale bar: 50 m. On the right-hand side, the wavelength-integrated *xy* and *xz* are shown. b) Summary of the lateral, δx, and axial, δz, resolution of the system as a function of the probing distance, z_0, after Richardson-Lucy deconvolution with ten iterations (to deduct the effect of finite probing samples), with linear and quadratic regressions, respectively. The error bars represent the standard deviation of N = 5 beads. The shaded region in orange represents the limits with both 22 and 27 m diameter beads. As the underwater probing distance increases, the shaded region converges to the average linear regression since the effect of the bead size on the PSF estimates continuously decreases (i.e., bead nears a δ-Dirac).

measurement to a near-diffraction limited probe volume. For each z, the relative spectrum of the bead is preserved, with a peak between 585.6 and 603.7 nm. The lateral PSF at different distances, as well as the spectrum of the beads at the centroid, are included in Figure S7 (Supporting Information).

To finalize, Figure 3b summarizes the deconvolved lateral, δx, and axial, δz, resolutions of the confocal LiDAR system as a function of the probing distance, z_0. The determination of δx from the PSF is described in Section 5. Both resolutions were estimated from the FWHM, according to the Rayleigh criterion. The lateral resolution of the system increases linearly from $\delta x \approx 20.26$ m at $z_0 \approx 548.10$ mm to $\delta x \approx 37.31$ m at $z_0 \approx 1090.50$ mm. For the same distances, the axial resolution increases quadratically from $\delta z \approx 3.86$ mm to $\delta z \approx 12.32$ mm. The probe volume, i.e., the volume excited by the laser beam and from which the inelastic signal is collected/integrated, is defined by the product $\delta x \times \delta z$ and is set by the overlap integral between the Gaussian beam and the profile of the pinhole backpropagated to the target plane.

3.2. Underwater Volumetric Multispectral Imaging

The multispectral confocal LiDAR system unlocks the possibility for underwater volumetric spectral imaging. To demonstrate the applicability in tridimensional measurements in the water column, we produced and imaged a depth-confined layer of polyethylene microbeads at the interface between a thick layer of distilled water and a layer of seawater (**Figure** 4a). Prior to sensing the scene, we created a library of independently acquired and labeled spectral samples of multiple beads, and trained an

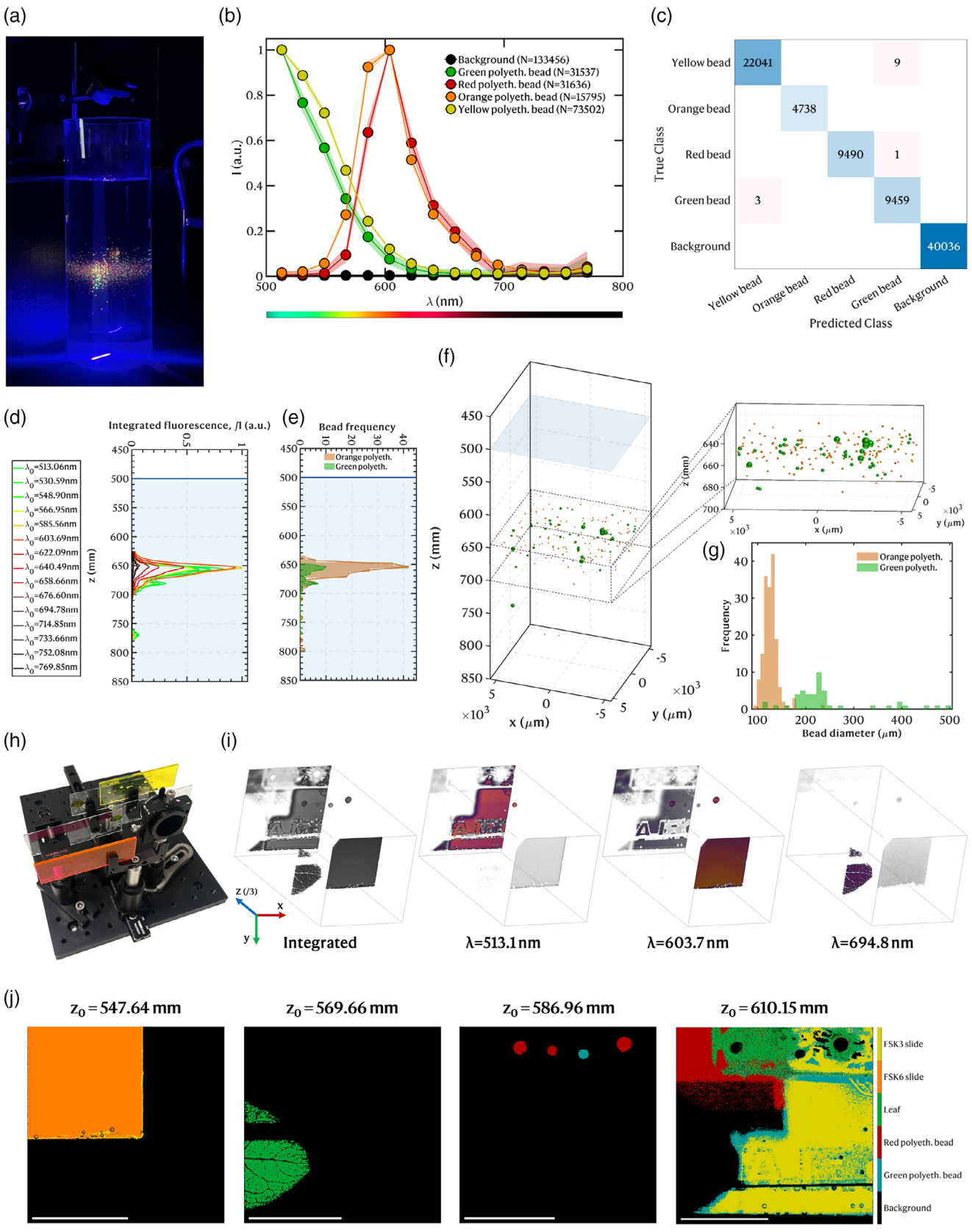

ensemble machine learning classifier using a random 70/30 split (training/testing). The average spectrum for each class of beads is displayed in Figure 4b, and the confusion matrix obtained after testing of the trained model is presented in Figure 4c. Although the spectra for the red/orange and yellow/green beads are similar, the signatures within the created dataset are almost completely distinguishable by the model. More information can be found in Section 5.

The results of the 3D reconstruction and analysis of the bead distributions are summarized in Figure 4d–g. The volumetric reconstruction of the layer is shown in Figure 4f, with the beads color-coded according to the class attributed by the AI model. Additionally, Figure 4d depicts the raw integrated fluorescence profiles as a function of the depth in the water column, z, obtained by integrating each z-plane image for each channel in separate, i.e., by summing the fluorescence for all the beads in each slice. Similarly, the bead color distribution with depth is represented in Figure 4e and is highly correlated with the previous fluorescence profiles, i.e., the peak in fluorescence at around 603 nm and at a depth $z \approx 650$ mm arises from a higher concentration of orange beads in the vicinity of this depth. The majority of the beads are concentrated at depths between 640 and 690 mm. A total of 216 microspheres are detected by the processing algorithm. Of these, 167 are orange, 46 green, one yellow, and two red. Since only green and orange beads were used to create the structured layer, the yellow and red beads represent misclassifications. Besides obtaining a distribution of the bead colors, it is also possible to create a distribution of the bead sizes, as demonstrated in the histogram in Figure 4g. The average size of the orange beads is 126.8 ± 16.1 m, which matches the nominal size provided by the manufacturer (106–125 m). As for the green beads, two nominal sizes have been used, 188–212 and 425-500 m, which approximately matches the estimates with the confocal LiDAR (a smaller group of beads with 207.7 m average diameter; infrequent bigger beads with sizes between 400–500 m).

With this experiment, we show that our novel multispectral LiDAR system is suitable for remote optical detection of microplastics in the water column. We showcase this for polyethylene, the dominant plastic used in industry.[45] This is particularly relevant since most plastics released into the ocean eventually disintegrate and break up into smaller particles that are now widespread in marine environments across the globe.[41] The small size of microplastic polluters (< 5 mm) makes them available to a wide range of marine biota.[46] For instance, ingestion of plastics by zooplankton adversely impacts their function and health,[46] and as a side effect reduces grazing of primary producers, which induces an additional anthropogenic driver for deoxygenation.[47] Therefore, there is a crucial drive to better understand the extent of microplastic proliferation in the oceans. In this sequence, our sensor opens the possibility for in situ and non-intrusive high-resolution mapping of plastic distributions ($\delta x \approx 22$ m for the distances used here), allowing us to sort them according to form, size, and color distributions using imaging spectroscopy.[32] Moreover, it can also replace subjective visual inspection methodologies that are often employed,[48] as the optical fingerprints provide an agnostic source for identification.

As an additional example of volumetric underwater imaging, we demonstrate the reconstruction of an artificial scene mimicking the one studied in ref. [21] with a single-channel system (Figure 4h). With the current LiDAR system, we extend the detection to obtain wavelength-resolved data, which allows us to reconstruct a volumetric render for each wavelength channel (Figure 4i) and to represent a spectrum for each voxel. This spectrum can then be used for spectral analysis of characteristic fingerprints and subsequent classification. For instance, the leaf sample exhibits a strong autofluorescence peak at around 700 nm, which is indicative of the presence of chlorophyll molecules.[49] An adaptive boosting model was trained on independently acquired signatures (see Figure S12, Supporting Information) and then applied to the best-focused images for each layer of the scene, to originate the segmented images in Figure 4j color-coded by class.

The confocal nature of the detection system enables the imaging through fluorescent layers to reveal objects that are otherwise blocked in the inelastic channels. For instance, part of the leaf at $z_0 = 569.66$ mm is hidden behind an FSK6 red fluorescent slide at $z_0 = 547.64$ mm. Whatsoever, since out-of-focus light is effectively suppressed spatially, the leaf is still detected and classified, without noticeable degradation of the wavefront and therefore the lateral resolution (veins still visible), as the slide is virtually eliminated from the analysis. Nonetheless, the fluorescence spectrum can be changed by intermediate objects in the optical path upon back propagation to the sensor, thus inducing misclassifications. For instance, at $z_0 = 586.96$ mm, the four beads shown are, from left to right, red, green, green, and red in color. The two leftmost beads are standing behind the red fluorescent slide, while the remaining two are unobstructed. As observable, the obstructed green bead is misclassified as a red bead, since the red fluorescence slide is not transparent in the green part of the electromagnetic spectrum (≈ 520 nm), thus changing the characteristic spectral signature of the green fluorescent bead, to one that resembles the red bead. The same is true for the obstructed portion of the FSK3 yellow fluorescent slide at the backplane $z_0 = 610.15$ mm. Examples of spectra for obstructed and unobstructed objects that illustrate this are included in Figure S16 (Supporting Information).

Figure 4. Volumetric underwater imaging. a) Photography of the structured layer of plastic microbeads created in the laboratory at the interface between a layer of distilled water and a layer of seawater. b) Library of spectral signatures acquired with four different bead colors. The solid line represents the mean signature, while the shaded areas represent the standard deviation. The number of averaged spectral points is disclosed in the legend for each class. c) Confusion matrix obtained after testing the ensemble classifier trained on 70% of the total spectral samples of each class. d) Integrated fluorescence profiles per spectral channel, as a function of the depth in the column of water, z. The blue line marks the water's surface. e) Depth distributions of each bead color. f) 3D reconstruction of the water column, with beads colored according to the class assigned by the ML model. A zoom-in of the bead layer is shown on the right-hand side. g) Histograms of the bead size distributions per color class. h) Photography of the artificial 3D scene assembled on an optical breadboard with multiple fluorescent objects. i) Volume render of the scene for the integrated wavelength channel, and three individual wavelength channels corresponding to the peak fluorescence of the yellow FSK3 slide and green beads ($\lambda = 513.1$ nm), the red FSK6 slide and red beads ($\lambda = 603.7$ nm), and the green leaf ($\lambda = 694.8$ nm). d) Montage of the segmented images of each layer, after background subtraction to remove out-of-focus contributions. Scale bar: 5 mm.

3.3. Imaging and Classification of Copepods

We demonstrate in vivo detection and classification of label-free, free-swimming copepods, and free-floating microalgae in a column of water, using the multispectral confocal LiDAR system. The laser probe was scanned in 3D (x, y, z), and, for each frame at a particular z-plane, a stack of spectral images was acquired. A photography of the water column is shown in **Figure 5a**, and a selection of detected autofluorescence events, i.e., microorganisms in the FOV, is shown in Figure 5b at different depths, z. Four species of sub-millimeter animals (zooplankton) in an adult stage are included in the mixture (*Acocyclops royi, Acartia tonsa, Temora longicornis*, and *Centropages hamatus*), as well as microalgae aggregates (phytoplankton). Copepods are sensitive bioindicators for changes in water quality,[50] and shifts in their communities provide sensitive indicators of climate change impacts on marine biotopes.[51] Hence, this group of small crustaceans is one of the most studied microorganisms in marine food webs. The size of adult copepods usually ranges from around 200 µm to 2 mm, and the concentrations can range up to 60,000 individuals per m^3 of water.[52]

As observable, since the sensor lateral resolution is well below the millimeter scale ($\delta x \approx 20$ m at these distances), it can detect spatial distributions of autofluorescence from sub-millimeter organisms, thus providing morphological information about shape and size of the specimens that are pivotal for classification.[53] Generally, all the imaged copepods exhibit broad bulk fluorescence, including from the antennae and the egg sacks for female *A. royi*, which is particularly strong in the central part of the body. However, as the organisms are free-swimming, they can appear with any orientation in the acquired frames, since the LiDAR images the projection of the copepod on the transverse probing plane (cross-section). Besides morphological features, the sensor system also locates and maps the organisms in 3D coordinates (x, y, z) relative to its referential, and performs laser-induced fluorescence spectroscopy that is a prominent cue to support classification.[25]

Figure 5c,d shows some examples of spectra from different pelagic microorganisms. In the leftmost plot in Figure 5d, we show signatures from two *C. hamatus* specimens and from different locations within the body to expose spatial variations in the emission spectrum according to local compositions that are captured by the LiDAR system. Notwithstanding, signatures can be very similar among different individuals of the same group. In the middle plot in Figure 5d, we compare the signatures of the four different zooplankton species to show spectral differences among them. For instance, the *A. royi 1* copepod has a broader fluorescence peak and shifted towards longer wavelengths (peak at $\lambda \approx 570$ nm), possibly due to differences in endogenous fluorophores. Nevertheless, all in all, the signatures match well the spectra obtained for identical zooplankton species in previous work using microspectrometry,[25] with a local fluorescence peak in the cyan at $\lambda \approx 500 - 550$ nm, likely due to a mixture of flavins, lipopigments, and/or NADH. Lastly, in the rightmost plot in Figure 5d, we show the signatures from the gut of a starved *A. royi* (2), plotted against the gut signal for a fed *A. royi* (3), and the autofluorescence from two microalgae aggregates. While the starved individual shows an autofluorescence signal with a single broad peak at around 550 nm, the fed individual simultaneously exhibits a peak at around 700 nm, strongly matching that of chlorophyll-containing phytoplankton aggregates. This indicates that the herbivorous organism had previously preyed on and has still to digest the microalgae.[54] Comparing the microalgae aggregates, a difference is noticeable as aggregate one has a broader red autofluorescence, which might indicate a separate species or disparity in pigmentation. In either case, the fluorescence shoulder at around 750 nm, characteristic of chlorophyll-*a* pigments, is resolved by the custom spectrometer and matches previously reported data.[55]

We collected and labeled spectral points from nine of the images, trying to include different spatial regions to capture intra-variability in local fluorescence among organisms belonging to either similar (e.g., due to status) or different species (see Figure S17 and Table S2, Supporting Information for the sample collection and distribution among classes). The average signatures for each class are shown in Figure 5e. We posteriorly trained a supervised machine learning model using a 70/30 split, i.e. using 70% of the datapoints of each class for training, and the remaining for testing of the classifier. Furthermore, we included spectral points from eight spatially disjoint images, to include test data from samples that have not been used for training. The error matrix comparing the classes assigned by the trained ensemble model and the ground truth provided by labeling is shown in 5f, normalized to the total number of samples per class due to the unbalanced dataset. Overall, all the classes are classified with high accuracy, with a minimum of 92.5% obtained for *C. hamatus*. As observable, the largest error rates arise from the misclassification of *A. royi* (4.8%), *C. hamatus* (5.5%), and *T. longicornis* (1.7%) as background pixels, likely due to non-uniformity in the bulk autofluorescence for these species and insufficient SNR in some spatial locations within the body. Among the living microorganisms, pixels belonging to *T. longicornis* are mistakenly classified as *A. royi* in 3.2% of the instances, while *C. hamatus* pixels are misclassified as *A. tonsa* at a 2.0% rate, due to spectral similarities. This pinpoints that the species can, in principle, be discerned based on spectrum alone. To conclude, Figure 5g shows the pixel-wise spectral classification results for all the images in the training and testing dataset. These results show, for the first time to our knowledge, that remote detection and identification is possible while reaching a favorable sensitivity and specificity using spectral features alone for the classes of micrometer-sized pelagic plankton studied herein, i.e., that the acquired spectroscopic data is useful for identification. The results also show that high-spectral resolution is not required, as implemented in other hyperspectral LiDAR instruments,[12] since fluorescence emission from biological targets is generally broad-banded and neighboring bands in high-spectral resolution systems are usually highly correlated, thus carrying less key valuable information.[56] Moreover, some of the copepod images yield very similar shapes and sizes when imaged by the system, which makes it hard to discriminate between species using form alone. In this sequence, we show herein that the spectrum provides an additional layer of information that is meaningful for classification.

Due to the limited amount of sample images, we based the automated classification solely on spectral features. However, detailed species identification requires morphology information. One can ideally integrate spectral detection with morphological

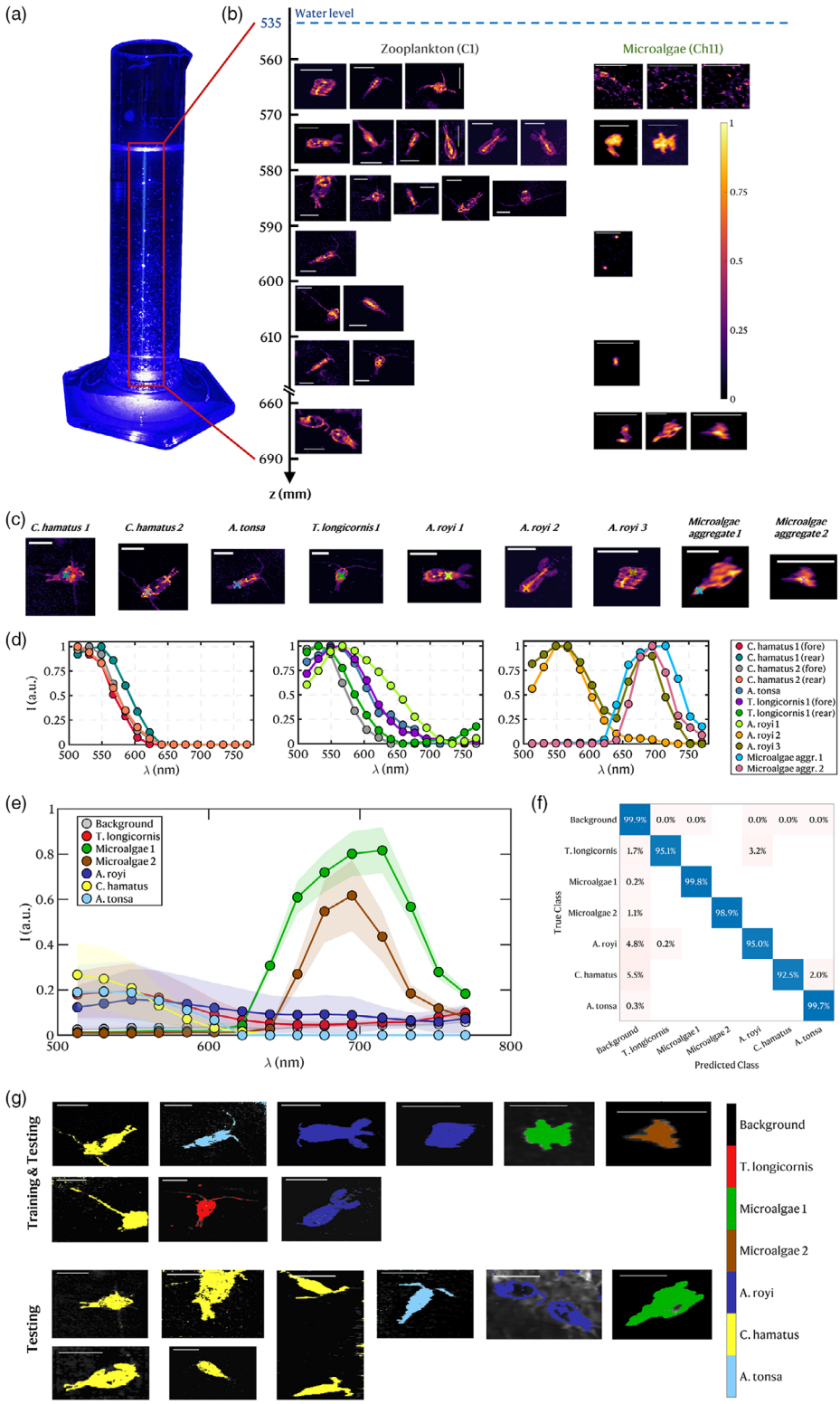

Figure 5. Confocal multispectral imaging of free-swimming microorganisms. a) Photography of the water cylinder used for measurements in a column of water. b) Example of events detected at different depths in the water column, *z*. For the zooplankton images, the image at the $\lambda = 513.1$ nm channel is shown; for the microalgae images (mostly aggregates), the image at $\lambda = 694.8$ nm is shown. c) Selected images, labeled according to classes. The crosses mark the spots from where spectrum samples were collected as an example for analysis. d) Examples of spectrum collected from different specimens. e) Assembled spectral library. The solid line represents the mean spectrum for each class; the shaded region marks the standard deviation. f) Normalized confusion matrix resulting from the application of the machine learning classifier to the testing dataset. g) Segmented images with class coded in color. Only the dominant class is overlayed with the grayscale images. Scale bars: 500 m.

data to perform spatial-spectral classification[31] and take advantage of the high-spatial-resolution information provided by the confocal LiDAR system. Spatial features like body shape, area, major and minor axes length, eccentricity, and perimeter, have proven to be key shape descriptors for accurate discrimination and classification.[8] Such an automated analysis unlocks rapid and objective digital recognition of copepods that is useful to both non-specialists and ecologists, removing human subjectivity from the identification pipeline. This requires a bigger training dataset that includes different shapes, orientations, and life cycle stages, acquired from spatially disjoint samples. This is notably demanding in underwater remote measurements with our LiDAR system, as the copepods can show in any location within the FOV and relative orientation, contrary to previous classification studies with neural networks using spatial data acquired under a microscope in which the copepods were physically rotated to have a specific dorsal aspect.[8]

4. Discussion and Outlook

To summarize, we have developed an inelastic confocal LiDAR for underwater remote volumetric multispectral imaging. This new instrument captures spatially referenced shape information with near diffraction-limited resolution, alongside pixel-level spectral data. The amalgamation of morphological data with species-specific spectroscopic information yields data-rich structures that can be used for automated classification using supervised machine learning models. In fact, we have accomplished laser-induced autofluorescence spectral imaging of micrometer-sized plastic beads, in vivo and free-swimming sub-millimeter zooplankton, and in vivo and free-floating phytoplankton aggregates in a column of water. We demonstrated in vivo spectral discrimination of six pelagic planktonic organisms. The optical fingerprints collected from each representative class provided a holistic and agnostic analysis using AI ensemble models, leading to an overall accurate identification. Furthermore, we have shown that due to the confocality of the excitation laser beam and the aperture pinhole, the sensor can selectively probe z-planes while inherently rejecting any out-of-focus light and scattering by design. This signifies that contributions from inelastic scatterers in intermediate layers outside the confocal volume are passively blocked with little to no degradation of the resolution,[40] making it a unique tool for optical surveying of aquatic biota and other suspended matter. This suppression extends background light sources, such as sunlight, although the reduction of its effects has not been quantified in this study as the system was implemented as a benchtop setup without adequate optical shielding of the detection path from stray light. However, preliminary tests on the influence of background lab lighting in a shielded single-detector configuration[21] show a small DC offset superimposed with the inelastic signal whose effect can be subtracted.

In the present design, we combine a fast and sensitive detector array with a 20 mm-diameter galvanometer dual-axis scanner and a remote focusing module to accomplish point-scan volumetric spectral imaging with short pixel integration times down to the $\approx$ 3 s order. Even with these swift dwell times, we could detect weak signals, including the low autofluorescence levels from highly transparent zooplankton.[6] This speed is currently limited by the maximum steering frequency of the fast axis, $f_x \approx 225$ Hz. On that account, an image with e.g., 450×450 pixels takes 1 s to be acquired as the construction is made pixel-by-pixel. Since plankton can appear at any position relative to the sensor, it is important to enhance the data throughput. The current MPPC detector has a bandwidth of 5 MHz, therefore there is a substantial margin to reduce the pixel dwell time down to $\sim$ 0.2 s and accomplish a frame rate at least 10 times greater for the same image resolution,[57] provided that the 16-channel ADC is properly replaced with a 10 MHz-range digitizer. The pixel rate can be improved by implementing a faster scanning system[58] or exploiting laterally or axially parallelized acquisition strategies,[59] such as tunable lenses.[60,61] Naturally, faster pixel dwell times translate into a deterioration of SNR as the inelastically backscattered photons are integrated for shorter periods at the detector. To compensate for this, the laser excitation power might be increased.

It is noteworthy to mention that, although we classify the system as multispectral in view of the number of channels and their spectral resolution, the measurement principle is hyperspectral regardless, since the fluorescence spectrum produced by the grating spectrograph is continuous.[62] The number of sampled wavelength bands is limited by the number of accessible digitizer and MPPC channels, chosen as a trade-off between the number of elements, bandwidth, and responsivity. Had more channels been available, a greater number of spectral bands could have been discriminated. Nonetheless, we have demonstrated that high-spectral resolution is not needed for spectral discrimination of biological targets studied herein as autofluorescence is broadband.

The proposed LiDAR system has currently only been operated in a confined laboratory environment, at distances from around 0.5 up to 1.1 meters, due to space restrictions. However, the remote-focusing system is compatible with short-range detection at up to more than 5 m. With effect, we plan to perform in the future the first in situ and layer-by-layer measurements in Danish coastal waters reaching depths consistent with this detection distance (depending on water clarity). At this distance, the lateral and axial resolutions can be extrapolated (using Figure 3b) to $\delta x \approx 156$ m and $\delta z \approx 250$ mm, meaning that the lateral resolution is preserved well below the millimeter mark, although the axial resolution is extended to integrate a larger layer of the water column. Therefore, further developments prompt improvements to the numerical aperture (NA) of the lens system to improve the spatiotemporal resolution and even extend the depth of view away from the sensor. A twofold increase in the NA of the system reduces δx and δz by a factor of two and four, respectively. Yet, such a photonic platform combined with artificial intelligence sets forth new instrumentation for in situ and non-intrusive studies of phytoplankton vertical profiles and zooplankton dynamics, interactions, and temporal changes in their spatial distributions in the water column. Moreover, studying the extent of microplastic contamination and its effects on the health of marine animals can improve our understanding of aquatic ecosystems. These investigations are particularly valuable given the critical ecological roles played by planktonic microorganisms, for instance in marine production cycles and as primary consumers in the food web.[46] If applied in the aquatic environment, as opposed to video methods,[19] the confocal LiDAR facilitates the acquisition of plankton abundance, taxonomy, and size through a potentially cost-effective approach in a single analysis with high temporal and spatial resolution, akin to the frequency at which

oceanographic measurements of the physical and chemical environment, such as chlorophyll or salinity, are made. The DoF of our system can be engineered, the probing distance can be remotely scanned, and the FOV can be electronically adjusted, thus allowing us to dynamically cover a varied range of volumes to obtain better statistical representations compared to fixed and limited DoF state-of-the-art technologies. Deployment options include installing the LiDAR sensor on a boat looking downward into the water column[14] for shallow-water surveys, or integration into vertical profiling instrumentation or submersible unmanned platforms, such as remotely operated vehicles (ROVs) and autonomous underwater vehicles (AUVs),[63] for deeper water surveys. This allows us to survey the water column remotely, thus circumventing the downsides of current techniques such as the need for a full dive of the instrumentation that inevitably escalates the logistical complexity of field campaigns. Therefore, this potentially opens up research that can intimately connect intricate biological variables to crucial biological information at the taxonomic level.

5. Experimental Section

Scanning and Imaging: Both axes of the galvanometer scanner were driven by triangular voltage signals to accomplish bi-directional scanning and acquisition. The waveform, angular FOV, frequency, offset, and phase of these signals were controlled independently on each axis (x and y) through a LabView graphic user interface. This flexibility allowed to tailor the scanning patterns to electronically zoom in or pan out specific regions of interest (ROIs),[57] and to control the pixel dwell times. The horizontal axis, x, was selected as the fast axis, scanned at a frequency f_x. The frame resolution was defined by the ratio between the fast and slow axis frequencies, f_x/f_y. The frame rate and pixel-dwell times were set by $2f_y$ and $f_y/(2f_x^2)$, respectively. The angular position feedback was sampled in real-time from the OPS output and converted into spatial position after digital low-pass filtering with cut-off $10f_x$ through a geometric transformation using the ranging equation and an optical magnification of $n_w \approx 1.33$ introduced by the refractive index mismatch between air and water.

Weighting Functions: A $400 \times 400 \times 1000\ mm^3$ (x, y, z) glass aquarium was filled with fresh tap water and positioned at a distance $z = d_{air} = 359$ mm from the objective lens L_2, with its 6 mm-thick flat glass walls orthogonal to the optical axis. Two fluorescent microscope slides were used to acquire the weighting functions of the instrument, to cover different sections of the spectral range of the instrument: a yellow slide (Thorlabs FSK3), and a red slide (Thorlabs FSK6). For a fixed probing distance, z_0, specified by the position of L_1, z_{piezo}, the slides were axially translated in 1 mm steps along the focused laser beam as the z-pixel size shall be set at least at one-third of the axial resolution.[44] For each position of the slide, a total of 2×10^6 samples were recorded over 1 s from each MPPC channel and averaged to yield an experimental intensity point. The data points, $I(z, \lambda)$, were then deconvolved with a 1.7 mm-thick rectangular pulse using the Richardson-Lucy algorithm[64] with ten iterations, to remove the effect of the slide thickness from the estimates. Finally, the experimental points were fit with a Lorentzian weighting function, $W(z) = I_0[1 + \left(\frac{z-z_0}{\delta z}\right)^2]^{-1}$, where I_0 is the height, and δz the FWHM and therefore the axial resolution according to the Rayleigh criterion. The AUC was then determined from the integral of the fit to estimate the absorption coefficient for each wavelength channel. The procedure was repeated for both slides at six different probing distances set by $z_{piezo} = 2.0, 13.0, 21.0, 27.0, 31.5, 36.5$ mm, covering an underwater probing distance from around 550 to 1100 mm. All distances were measured with a rangefinder (Bosch GLM 250VF, 1 mm accuracy) and were referenced to L_2. A constant power of 6.5 mW (FSK6) and 0.65 mW (FSK3) was used throughout the measurements to apply a universal normalization and conclude about absorption. All measurements were performed in a dark laboratory since the MPPC detector was not optically shielded from stray background light.

Lateral PSF: Fluorescent red polyethylene microspheres with 22–27 m diameter (Cospheric UVPMS-BR-0.9995) were used as probes for the lateral PSF. Several beads were attached to a microscope glass slide using double-sided tape and mounted directly underwater to avoid additional interfaces. For the same z_{piezo} positions, the slide was translated on a linear stage across the laser probe. $750 \times 750 \times 15$ (x, y, λ) spectral images were acquired at each z-position with a pixel dwell time of 4.44 s and over a $0.25^o \times 0.25^o$ angular FOV. The pixel size was at least six times smaller than the lateral resolution to ensure a suitable spatial sampling frequency, according to the Nyquist limit.[44] The optical power was increased with distance from 12.2 mW to 16.3 mW to obtain a good SNR without photobleaching. From the resulting 4D stack of images, $I(x, y, z, \lambda)$, $50 \times 50 \times 15$ ROIs was cropped to isolate single beads, and each spectral image was filtered with a bi-dimensional Gaussian kernel (5×5 pixels, $\sigma = 1.25$), to correct scanning artifacts and reconstruction noise. Subsequently, the lateral PSF was selected as the best focus image, i.e., the image acquired at a z-axis position matching the focal plane of the system, and all the spectral channels were integrated into a single normalized image, $I(x, y)$. A least-mean squares Gaussian fit was then applied to the horizontal integrated intensity profile, $G(x) = I_0 \exp\left(-\frac{(x-b)^2}{2c^2}\right)$, were a, b, and c were fitting parameters. The FWHM of the PSF was computed, $\delta x = 2c\sqrt{2\ln 2}$, and used to quantify the resolution of the system, again according to the Rayleigh criterion. At last, Richardson-Lucy deconvolution with ten iterations was applied with two 2D Gaussian kernels with full-width at tenth-maximum of 22 and 27 m to deduct the effect of the bead sizes from the δx estimates while considering their size distributions. The average of the two estimates was considered. For each probing distance, this procedure was repeated for N = 5 microspheres.

Supervised Artificial Intelligence Models: All classification tasks were performed pixel-wise using an ensemble supervised machine learning algorithm purely trained on spectral features. More specifically, an adaptive boosting (AdaBoost.M2) method was used to build a classifier for each problem showcased in this paper. For each decision tree, a maximum number of 20 splits was selected. The total number of learners was 30, with a learning rate of 0.1. This method was used due to the reduced bias and variance, providing good accuracy and resistance to overfitting. No hyperparameter optimization was performed, and all 15 spectral bands were used (i.e., no dimensionality reduction).

Volumetric Imaging of an Artificial Scene: An artificial scene similar to the one used in ref. [21] was recreated to demonstrate the extended capabilities of a multispectral confocal LiDAR system compared to a single-band system. A total of four layers with different autofluorescent objects were assembled on an optical breadboard and along the optical axis: a red fluorescent microscope slide (Thorlabs FSK6); a green leaf, partially obstructed by the first layer; two red (Cospheric UVPMS-BR-0.995 710–850 m) and two green (Cospheric UVPMS-BG-1.00 425–500 m) fluorescent polyethylene beds, one of each obstructed by the first slide; a yellow fluorescent microscope slide (Thorlabs FSK3). The breadboard was placed inside the aquarium and a stack of $800 \times 800 \times 157 \times 15$ (x, y, z, λ) images was acquired step-wise from $z_{piezo} = 0.0$ mm to $z_{piezo} = 16.0$ mm with a minimum increment $\delta z_{piezo} = 50\ \mu m$ (accuracy of the piezoelectric stage), corresponding to an underwater probing distance from around 535 to 680 mm. An angular FOV of $1.2^o \times 1.2^o$ was scanned at a pixel rate of 320 kHz. The excitation laser beam power was kept at 2.2 mW throughout all acquisition and each MPCC channel was sampled at 1 MHz. Subsequently, the following processing workflow was applied: 1) subtraction of the background offset, median filtering (3×3 kernel), and normalization; 2) pixel-level peak detection to find the best focus images (see Figure S13, Supporting Information); 3) binary masking to remove out-of-focus contributions (see Figure S14, Supporting Information); 4) pixel-wise classification; 5) 3D rendering. The samples for training the classifier were obtained by labeling independent images of each object (see Figure S12,

Supporting Information). The background suppression process is illustrated in Figures S14 and S15 (Supporting Information).

Volumetric Imaging of A Spatially-Confined Layer of Microplastics: The glass aquarium was replaced by an acrylic cylindrical container with a 150 mm cross-section diameter and 500 mm height. The laser was deflected 90° using a pair of broadband dielectric mirrors (Thorlabs BB2-E02) to perform measurements vertically in a column of water (i.e., z-axis along depth). A controlled flow of distilled water was pumped into the cylinder from the bottom up through a tube. Then, a mixture of beads suspended in water was carefully injected in the same way while preventing the formation of air bubbles. Three different types of plastic microspheres were used: two fluorescent green polyethylene beads with different sizes (Cospheric, UVPMS-BG-1.00 188–212 and 425–500 m), and a fluorescent orange polyethylene (Cospheric, UVPMS-BO-1.00 106–125 m), all with a density of 1.00 gcm^{-3}. Ultimately, seawater was introduced to push the full structure up. A suspended layer of microplastics confined in depth to the interface between the distilled and seawater (mixed layer) was thus created. For the volumetric measurements, the water surface was placed at a distance $z = d_{air}$= 500 mm from L_2 and left undisturbed for 12 hours to allow the configuration to reach a static equilibrium. Afterward, a stack of 237 spectral images was collected at incremental z_{piezo} positions, which were then converted into z_0 using the ranging equation. At each depth, $800 \times 800 \times 15$ (x, y, λ) transverse images were acquired with a pixel dwell time of 3.125 s and over an angular FOV of $1^o \times 1^o$. The laser was run at 1.5 mW and all ADC channels were sampled at 1 MHz. The image processing workflow is summarized in Figure S8 (Supporting Information). The images were first background subtracted, median filtered (3×3), and normalized to the maximum of the full stack. A circular Hough transform was applied to detect the edges of the beads, taking advantage of their spherical symmetry. A peak detection algorithm was implemented to determine the z-position of each microsphere, i.e., the depth at which the signal peaked and the bead was in focus. From this, a 3D binary mask was created to suppress out-of-focus contributions arising from the axial roll-off of the weighting functions and applied pixel-wise classification followed by a maximum abundance vote, since each bead belongs to a single class. Conclusively, the 3D scene was constructed and the bead size and color distributions were computed. Multiple spectral data points were obtained separately from spatially disjoint samples to create a training dataset. Several beads were glued to a microscope slide with double-sided tape and images were taken in air. The images were then labeled manually to create a spectral library (see Figure S9, Supporting Information for an example). Besides the three bead types aforementioned, samples were also acquired for yellow polyethylene beads (UVPMS-BY2-1.00 300-355 m) and red polyethylene beads (Cospheric UVPMS-BR-0.995 710–850 m) with identical spectra (see Figure 4b) to further expand the pool of potential classes for the machine learning model.

Label-Free Plankton Imaging: Four different pelagic zooplankton species, more specifically planktonic copepods in an adult stage, were independently cultured in lab conditions and kept in brackish water: *Acocyclops royi*, *Acartia tonsa*, *Temora longicornis*, and *Centropages hamatus*. Prior to the experiments, multiple samples of these four microorganisms were transferred alongside phytoplankton to a glass cylinder to create a mixed medium. All the species were starved prior to the acquisitions, with the exception of the *A. royi*, which comprised both starved and microalgae-fed specimens. Several $750 \times 750 \times 15$ images were acquired at different depths over $0.6^o \times 0.6^o$ FOVs, at a pixel dwell time of $\approx$ 3 s and with an excitation beam power of 72.5 mW. The depth-resolved spectral images were then processed as follows: 1) background subtraction; 2) selection of images where events were identified, i.e., images that contain copepods; 3) cropping of the ROIs corresponding to individual events; 4) denoising using a pre-trained convolutional neural network; 5) filtering with a 3D box filter; 6) unsharp masking; 7) normalization, while keeping relative intensity between spectral channels; 8) spectral classification. Due to a limited amount of sample images and, therefore, spectra for classification, some of the images were simultaneously used for training and testing, while saving a part of the remaining as a spatially disjoint test dataset. The first set of images was manually labeled (see Figure S17, Supporting Information) to create a ground truth, and the data points were randomly split using a random 70/30 ratio to generate the training and test datasets, respectively. Since the full dataset was unbalanced, the division was performed individually class-wise to guarantee the same representation of samples in both sets.

Supporting Information

Supporting Information is available from the Wiley Online Library or from the author.

Conflict of Interest

The authors declare no conflict of interest.

Data Availability Statement

The data that support the findings of this study are available from the corresponding author upon reasonable request.

Keywords

autofluorescence, automatic plankton identification, machine learning, multispectral LiDAR, spectral classification, underwater volumetric confocal imaging

Received: December 16, 2023
Revised: May 7, 2024
Published online: May 25, 2024

[1] S. L. Deppeler, A. T. Davidson, *Front. Mar. Sci.* **2017**, *4*, 40.
[2] L. A. Levin, N. Le Bris, *Science* **2015**, *350*, 766.
[3] E. S. Poloczanska, C. J. Brown, W. J. Sydeman, W. Kiessling, D. S. Schoeman, P. J. Moore, K. Brander, J. F. Bruno, L. B. Buckley, M. T. Burrows, C. M. Duarte, B. S. Halpern, J. Holding, C. V. Kappel, M. I. O'Connor, J. M. Pandolfi, C. Parmesan, F. Schwing, S. A. Thompson, A. J. Richardson, *Nat. Clim. Change* **2013**, *3*, 919.
[4] J.-P. Gattuso, A. Magnan, R. Billé, W. W. L. Cheung, E. L. Howes, F. Joos, D. Allemand, L. Bopp, S. R. Cooley, C. M. Eakin, O. Hoegh-Guldberg, R. P. Kelly, H.-O. Pörtner, A. D. Rogers, J. M. Baxter, D. Laffoley, D. Osborn, A. Rankovic, J. Rochette, U. R. Sumaila, S. Treyer, C. Turley, *Science* **2015**, *349*, aac4722.
[5] F. Lombard, E. Boss, A. M. Waite, M. Vogt, J. Uitz, L. Stemmann, H. M. Sosik, J. Schulz, J.-b. Romagnan, M. Picheral, J. Pearlman, M. D. Ohman, B. Niehoff, K. O. Möller, P. Miloslavich, A. Lara-Lpez, R. Kudela, R. M. Lopes, R. Kiko, L. Karp-Boss, J. S. Jaffe, M. H. Iversen, J.-O. Irisson, K. Fennel, H. Hauss, L. Guidi, G. Gorsky, S. L. C. Giering, P. Gaube, S. Gallager, et al., *Front. Mar. Sci.* **2019**.
[6] M. Brydegaard, S. Svanberg, *Laser Photonics Rev.* **2018**, *12*, 1800135.
[7] K. Bandara, Ø. Varpe, L. Wijewardene, V. Tverberg, K. Eiane, *Biol. Rev.* **2021**, *96*, 1547.
[8] L. K. Leow, L. L. Chew, V. C. Chong, S. K. Dhillon, *BMC Bioinformatics* **2015**, *16*, 1.
[9] H. Lee, M. Park, J. Kim, *2016 IEEE International Conference on Image Processing (ICIP)*, Phoenix, AZ, USA, **2016**, pp. 3713–3717.
[10] M. J. Behrenfeld, Y. Hu, R. T. O'Malley, E. S. Boss, C. A. Hostetler, D. A. Siegel, J. L. Sarmiento, J. Schulien, J. W. Hair, X. Lu, S. Rodier, A. J. Scarino, *Nat. Geosci.* **2017**, *10*, 118.
[11] M. J. Behrenfeld, P. Gaube, A. Della Penna, R. T. O'Malley, W. J. Burt, Y. Hu, P. S. Bontempi, D. K. Steinberg, E. S. Boss, D. A. Siegel, C. A. Hostetler, P. D. Tortell, S. C. Doney, *Nature* **2019**, *576*, 257.

[12] G. Zhao, M. Ljungholm, E. Malmqvist, G. Bianco, L. A. Hansson, S. Svanberg, M. Brydegaard, *Laser Photonics Rev.* **2016**, *10*, 807.
[13] S. Sunagawa, S. G. Acinas, P. Bork, C. Bowler, M. Babin, E. Boss, G. Cochrane, C. de Vargas, M. Follows, G. Gorsky, N. Grimsley, L. Guidi, P. Hingamp, D. Iudicone, O. Jaillon, S. Kandels, L. Karp-Boss, E. Karsenti, M. Lescot, F. Not, H. Ogata, S. Pesant, N. Poulton, J. Raes, C. Sardet, M. Sieracki, S. Speich, L. Stemmann, M. B. Sullivan, P. Wincker, et al., *Nat. Rev. Microbiol.* **2020**, *18*, 428.
[14] Y. Zhou, Y. Chen, H. Zhao, C. Jamet, D. Dionisi, M. Chami, P. Di Girolamo, J. H. Churnside, A. Malinka, H. Zhao, D. Qiu, T. Cui, Q. Liu, Y. Chen, S. Phongphattarawat, N. Wang, S. Chen, P. Chen, Z. Yao, C. Le, Y. Tao, P. Xu, X. Wang, B. Wang, F. Chen, C. Ye, K. Zhang, C. Liu, D. Liu, *Light: Sci. Appl.* **2022**, *11*, 1.
[15] M. Shangguan, Z. Yang, Z. Lin, Z. Lee, H. Xia, Z. Weng, *IEEE Geosci. Remote Sens. Lett.* **2023**, *20*, 1.
[16] R. J. Olson, A. Shalapyonok, H. M. Sosik, *Deep-Sea Res. Part I: Oceanogr. Res. Pap.* **2003**, *50*, 301.
[17] Z. Liu, T. Takahashi, D. Lindsay, T. Thevar, M. Sangekar, H. K. Watanabe, N. Burns, J. Watson, B. Thornton, *IEEE J. Oceanic Eng.* **2021**, *46*, 1248.
[18] M. Picheral, C. Catalano, D. Brousseau, H. Claustre, L. Coppola, E. Leymarie, J. Coindat, F. Dias, S. Fevre, L. Guidi, J. O. Irisson, L. Legendre, F. Lombard, L. Mortier, C. Penkerch, A. Rogge, C. Schmechtig, S. Thibault, T. Tixier, A. Waite, L. Stemmann, *Limnol. Oceanogr.: Methods* **2022**, *20*, 115.
[19] S. M. Gallager, C. S. Davis, A. W. Epstein, A. Solow, R. C. Beardsley, *Deep-Sea Res. Part II: Top. Stud. Oceanogr.* **1996**, *43*, 1627.
[20] A. D. Mullen, T. Treibitz, P. L. Roberts, E. L. Kelly, R. Horwitz, J. E. Smith, J. S. Jaffe, *Nat. Commun.* **2016**, *7*, 1.
[21] J. Santos, P. J. Rodrigo, P. M. Petersen, C. Pedersen, *Sci. Rep.* **2023**, *13*, 4807.
[22] A. Lumini, L. Nanni, *Ecol. Inf.* **2019**, *51*, 33.
[23] Z. Ling, D. Sun, S. Wang, Z. Qiu, Y. Huan, Z. Mao, Y. He, *Opt. Express* **2018**, *26*, 30556.
[24] B. Greg Mitchell, D. A. Kiefer, *Deep Sea Res. Part A. Oceanogr. Res. Pap.* **1988**, *35*, 639.
[25] J. H. Nielsen, C. Pedersen, T. Kiørboe, T. Nikolajsen, M. Brydegaard, P. J. Rodrigo, *Appl. Opt.* **2019**, *58*, 7022.
[26] X. Chen, Y. Jiang, Q. Yao, J. Ji, J. Evans, S. He, *Appl. Opt.* **2021**, *60*, 4778.
[27] A. F. H. Goetz, G. Vane, J. E. Solomon, B. N. Rock, *Science* **1985**, *228*, 1147.
[28] B. Liu, Z. Liu, S. Men, Y. Li, Z. Ding, J. He, Z. Zhao, *Sensors* **2020**, *20*, 4962.
[29] G. Lu, B. Fei, *J. Biomed. Opt.* **2014**, *19*, 010901.
[30] A. Chennu, P. Färber, G. De'ath, D. De Beer, K. E. Fabricius, *Sci. Rep.* **2017**, *7*, 1.
[31] Y. Chen, H. Jiang, C. Li, X. Jia, P. Ghamisi, *IEEE Trans. Geosci. Remote Sens.* **2016**, *54*, 6232.
[32] A. Faltynkova, G. Johnsen, M. Wagner, *Microplast. Nanoplast.* **2021**, *1*, 1.
[33] J. Luo, H. Zhang, E. Forsberg, S. Hou, S. Li, Z. Xu, X. Chen, X. Sun, S. He, *Opt. Express* **2021**, *29*, 37281.
[34] I. Dumke, A. Purser, Y. Marcon, S. M. Nornes, G. Johnsen, M. Ludvigsen, F. Søreide, *Sci. Rep.* **2018**, *8*, 12860.
[35] D. B. Lindell, G. Wetzstein, *Nat. Commun.* **2020**, *11*, 1.
[36] J. A. Conchello, J. W. Lichtman, *Nat. Methods* **2005**, *2*, 920.
[37] Y. Sung, W. Wang, *Opt. Lett.* **2023**, *48*, 3993.
[38] M. B. Sinclair, D. M. Haaland, J. A. Timlin, H. D. Jones, *Appl. Opt.* **2006**, *45*, 6283.
[39] M. Levoy, B. Chen, V. Vaish, M. Horowitz, I. McDowall, M. Bolas, *ACM SIGGRAPH 2004 Papers, SIGGRAPH 2004* **2004**, *1*, 825.
[40] J. Santos, D. Koestner, Y.-C. Chen, P. J. Rodrigo, P. M. Peteresen, B. Hamre, C. Pedersen, *OCEANS 2023 - Limerick*, **2023**, pp. 1–10.
[41] A. L. Andrady, *Mar. Pollut. Bull.* **2011**, *62*, 1596.
[42] R. M. Pope, E. S. Fry, *Appl. Opt.* **1997**, *36*, 8710.
[43] T. Wilson, A. R. Carlini, *Opt. Lett.* **1987**, *12*, 227.
[44] R. W. Cole, T. Jinadasa, C. M. Brown, *Nat. Protoc.* **2011**, *6*, 1929.
[45] R. Geyer, J. R. Jambeck, K. L. Law, *Sci. Adv.* **2017**, *3*, 25.
[46] M. Cole, P. Lindeque, E. Fileman, C. Halsband, R. Goodhead, J. Moger, T. S. Galloway, *Environ. Sci. Technol.* **2013**, *47*, 6646.
[47] K. Kvale, A. E. F. Prowe, C.-T. Chien, A. Landolfi, A. Oschlies, *Nat. Commun.* **2021**, *12*, 2358.
[48] V. Hidalgo-Ruz, L. Gutow, R. C. Thompson, M. Thiel, *Environ. Sci. Technol.* **2012**, *46*, 3060.
[49] J. Santos, M. L. Pedersen, B. Ulusoy, C. E. Weinell, H. C. Pedersen, P. M. Petersen, K. Dam-Johansen, C. Pedersen, *Sensors* **2022**, *22*, 1.
[50] A. Albaina, F. Villate, I. Uriarte, *J. Plankton Res.* **2009**, *31*, 739.
[51] M. Edwards, A. J. Richardson, *Nature* **2004**, *430*, 881.
[52] L. L. Chew, V. C. Chong, *Hydrobiologia* **2011**, *666*, 127.
[53] H. M. Sosik, R. J. Olson, *Limnol. Oceanogr.: Methods* **2007**, *5*, 204.
[54] E. M. Karaköylü, P. J. S. Franks, Y. Tanaka, P. L. D. Roberts, J. S. Jaffe, *Limnol. Oceanogr.: Methods* **2009**, *7*, 33.
[55] Y. Saito, K. Takano, F. Kobayashi, K. Kobayashi, H.-D. Park, *Appl. Opt.* **2014**, *53*, 7030.
[56] C. Rodarmel, J. Shan, *Surv. Land Inf. Sci.* **2002**, *62*, 115.
[57] J. Jonkman, C. M. Brown, *J. Biomol. Techn.* **2015**, *26*, 54.
[58] S. Choi, P. Kim, R. Boutilier, M. Y. Kim, Y. J. Lee, H. Lee, *Opt. Express* **2013**, *21*, 23611.
[59] J. Mertz, *Optica* **2019**, *6*, 1261.
[60] J. M. Jabbour, B. H. Malik, C. Olsovsky, R. Cuenca, S. Cheng, J. A. Jo, Y.-S. L. Cheng, J. M. Wright, K. C. Maitland, *Biomed. Opt. Express* **2014**, *5*, 645.
[61] E. Mcleod, A. B. Hopkins, C. B. Arnold, *Opt. Lett.* **2006**, *31*, 3155.
[62] T. Hakala, J. Suomalainen, S. Kaasalainen, Y. Chen, *Opt. Express* **2012**, *20*, 7119.
[63] O. Sture, M. Ludvigsen, F. Soreide, L. M. S. Aas, *OCEANS 2017 - Aberdeen*, **2017**, pp. 1–8.
[64] D. A. Fish, J. G. Walker, A. M. Brinicombe, E. R. Pike, *J. Opt. Soc. Am. A* **1995**, *12*, 58.